PROTOTYPE RESULTS OF A HIGH RESOLUTION VERTEX DRIFT CHAMBER FOR THE MARK II SLC UPGRADE DETECTOR[*]

J. Alexander, K. Hayes, C. Hoard,

D. Hutchinson, J. Jaros, S. Odaka,[§] R. Ong

Stanford Linear Accelerator Center
Stanford University, Stanford, California 94305

P. Drell, R. Fuzesy, R. Harr, G. Trilling

Lawrence Berkeley Laboratory and Department of Physics
University of California, Berkeley, California 94720

ABSTRACT

Test results from a full-length prototype of the drift chamber vertex detector for the Mark II SLC Upgrade detector are presented. The 22 cell jet chamber employs planes of grid wires above and below the sense wire plane to increase the electrostatic stability of the sense wires and to narrow the electron arrival time distribution. Two different grid designs have been investigated. The spatial resolution and pulse widths have been measured at a variety of operating points and for different timing schemes in a mixture of 92% CO_2 and 8% isobutane. Typical results at 3 atmospheres pressure give an average resolution over a 2 cm drift distance of 30 μm for both designs. Efficient double track detection is achieved for tracks separated by 500 μm for one design and by 1000 μm for the other.

Presented at the Wire Chamber Conference,

Vienna, Austria, February 25-28, 1986

Introduction

Vertex detectors will enhance studies of Z^0 decays by identifying heavy quark flavors, measuring heavy quark and lepton lifetimes, and searching for new particles that give rise to distinct decay vertices. We are developing a high resolution drift chamber vertex detector for the Mark II Upgrade Detector to be used at the Stanford Linear Collider at SLAC[1]. Our design attempts to optimize spatial resolution in a structure capable of discriminating between the closely-spaced tracks characteristic of high energy hadronic jets[2].

The double track separation capability of a chamber is determined by the width of the electron arrival time distribution at the sense wire. There are two main contributions to this width: non-isochronous charge collection and electron diffusion. Non-isochronous charge collection results from the fact that ionization electrons produced by the passage of charged particles through the gas travel different distances and through different electric fields to reach the sense wire, depending on where they were produced. The drift differences are proportional to the track length which is sampled, and depend on the angle of the track in the chamber. The broadening due to diffusion is determined by the gas chosen for the chamber and, as in the case of spatial resolution, can be minimized by pressurized operation.

To achieve the required sub-millimeter track-pair resolution, we have used jet-cell[3] geometries with tightly spaced sense wires straddled by planes of grid wires, which focus the incoming ionization and stabilize the array against electrostatic forces. To ease the electronic difficulties in timing closely spaced pulses, we use CO_2/isobutane at unsaturated drift velocities[4]. Prototype chambers have been operated at several atmospheres pressure in order to achieve high spatial resolution. Particular attention is paid to very precise wire location and the high voltage isolation of closely spaced wires.

In the remainder of this paper, we discuss the following topics: (1) drift-cell description; (2) mechanical construction; (3) test apparatus; (4) data analysis

proceedure; (5) pulse shape measurements; (6) spatial resolution measurements; and (7) track-pair resolution studies.

I. DRIFT CELL DESCRIPTION

We have prototyped two drift cell designs which are illustrated in Fig. 1. The "wide" grid design is shown in Fig. 1(a). Sense wires are spaced 4 mm apart and have potential wires between them. Grid wires are parallel to the anode plane and are located directly over the potential wires. In this wide grid design, the 4 mm sense spacing determines the length of the ionization segment that arrives at the sense wire. The electron drift trajectories for this design are shown in Fig. 2(a). Our second prototype cell, the "narrow" grid design, is illustrated in Fig. 1(b). This design also has 4 mm sense wire spacing but the grids are quite different. There are three types of grid wires in this cell, each connected to a separate voltage. When voltages are suitably arranged the middle grid wire is positively charged, and the resulting drift trajectories are as shown in Fig. 2(b). Only the electrons from the track segment above the two inner grid wires are collected at the anode. As a result the length of track sampled is only 1.2 mm. In this design the charge on the inner grid wire can be adjusted to optimize the focusing of the cell.

The isochrony of the charge collection for the two cell designs is illustrated in Fig. 3 which shows typical lines of constant drift time in the uniform drift field region of the cells. For the narrow grid cell in the absence of diffusion, most ionization electrons will arrive at the sense wire within a few hundred μm of the first one although a small fraction may arrive up to 700 μm late. These dimensions for the wide grid cell are about three times larger. Primary ionization cluster fluctuations in these late regions of the cell will be visible in the pulse tails if the diffusion is small compared to these dimensions.

II. MECHANICAL CONSTRUCTION

Our test chambers have 22 drift cells with wires 60 cm long and parallel

planar cathodes made of copper-clad G-10, spaced 3 cm from each grid plane. The wire planes are fabricated by winding wires between a pair of 2-inch diameter copper-coated invar cylinders. Fine grooves with precisely controlled depth and spacing are machined into the cylinders to fix relative wire positions with great accuracy. Fig. 4 shows measurements of wire positions, indicating rms errors of 1 μm in the plane of the wires, and 5 μm out of the plane, the latter result being dominated by measurement error. Once wound, a wire plane is epoxied, as a unit, into the chamber. This technique ensures that the positional accuracy inherent in the cylinders is transferred to the chamber. Wire tensions are set during the winding, 60 g for the 20 μm tungsten sense wires, and 450 g for the 152 μm copper-beryllium grid and potential wires. Measured tensions show an rms error of 1% about the mean, with no detectable change after 3 months of operation.

Fig. 5 schematically illustrates the wire plane terminations. The anode plane is epoxied to a block of Macor, a machinable glass with excellent dielectric characteristics, and soldered to circuitry also epoxied to the Macor surface. After soldering, the circuits are cleaned and potted with additional epoxy. At the front face of the Macor, each wire passes through a notch that serves as a high voltage feedthrough into the active volume of the chamber, permitting large voltage differences between adjacent wires. The circuitry for the narrow grid is printed on thin copper clad Kapton. The solder pads can be kept very small, and tiny (225 μm) plated-through holes connect to voltage busses on the underside.

Overall structural support and rigidity is provided by aluminum frames to which the Macor blocks are screwed and pinned. The precise alignment of one wire plane relative to another is achieved during construction by use of a microscope mounted on an $x - y - z$ stage. Under the microscope, positions can be measured with micron-level accuracy. Measurements of the wire planes after assembly indicate deviations from nominal positions of approximately 15 μm or less.

III. APPARATUS

The chamber is run in an aluminum pressure vessel inside a cosmic ray telescope. The gas (92% CO_2, 8% isobutane) flows through the chamber at .3 scfh and oxygen and water are removed with an in-line Oxisorb filter. Electron lifetimes in the chamber typically exceed 30 μs. The center 8 wires are instrumented with Plessey SL560 current sensitive preamps mounted directly on the chamber. The sense wires are at ground and typical grid and potential wire voltages are about -3500 volts. Voltage differences for the 3 narrow grid planes are in the few hundred volt range.

The threshold timing measurements are made using a LeCroy MVL-100 amplifier/discriminator followed by a system of "fast" and "slow" TDC's (LeCroy 2228). The clock for the slow TDC is started by a hit in the cosmic ray telescope and these slow times measure drift times up to 5 μsec with 2.5 nsec bins. The first wire hit starts the fast TDC's which have a time range of 500 nsec in 250 psec bins and are used to measure actual resolutions.

In addition to the TDC system, there are six channels instrumented with a postamp followed by 100 MHz image chamber analyzer (LeCroy 2261 ICA) with 11 bit resolution. The postamp consists of a two stage pole zero filter followed by two stages of SL560's with a net gain of 40. A hit in the cosmic ray telescope provides a synchronization pulse to the postamp which is used to measure the phase of the ICA clock on each channel.

IV. ANALYSIS PROCEEDURE

The measured drift times are converted to drift distance using a linear drift time-distance relationship. Drift distances are measured with respect to the grid plane; hits from the region between the anode and grid planes are ignored. The drift velocity is obtained by measuring the difference between the drift time for tracks which cross the cathode surface and those which cross the grid plane.

Several cuts are made to improve the quality of the track sample. First a

linear fit is made to the hit data from the 8 TDC channels. The individual fit residuals are scaled to yield the correct measurement error for each wire. Hits whose residual is larger than 10 times the expected resolution are dropped and the fit is repeated. Tracks with fewer than 5 good hits or which make an angle larger than 200 mrad to the anode plane are rejected. Wire inefficiencies are less than 1 percent.

For the average pulse shape and spurious hit rate studies, additional cuts are made on the ICA data to ensure only one track traversed the chamber. A hit in the ICA data is recognized as two or more contiguous ICA bins above threshold (3.5 times rms noise level). Hits separated by fewer than 10 bins are merged. Tracks are rejected if more than 4 of the ICA channels have multiple hits or if the sum of the 4 smallest wire pulse heights is consistent with two or more tracks in the chamber.

V. AVERAGE PULSE SHAPE

The average pulse shapes from the narrow and wide grid structures are shown in Fig. 6. We construct these distributions from the ICA data as follows. For each pulse we compute a total pulse height, and using an algorithm discussed below, a mean time. A track fit to the times from all six wires then gives a fitted mean time to each pulse. Each bin of the ICA data is then assigned a fractional pulse height, normalized to the total for the pulse, and an arrival time computed with respect to the fitted mean time. The average of these fractional pulse heights for a large ensemble of tracks is simply binned in arrival time to give the distributions shown in the figure. The root-mean-square deviation of the pulse heights is also determined for each arrival time bin, and is plotted as the "error" on each point.

Several features of the pulse shapes are worth noting. The arrival time distribution of the narrow grid is considerably narrower than that of the wide grid, the latter having a long tail of late arriving ionization. Using the measured drift velocity, we see that the effective pulse widths of the narrow grid design are at

the 500 μm level, whereas those for the wide grid extend to around 1500 μm. The effects of diffusion are evident when we contrast the pulse shapes coming from $\leq$ 5 mm drifts to those coming from $>$ 25 mm drifts. The pulse width and the rise time both increase with increasing drift distance. Pulse widths will also increase for tracks making an angle with respect to the sense plane. This effect is negligible in this data since the range of track angles is small. Finally, we note that the tails of the distributions of pulses in the wide grid chamber show large fluctuations, the rms deviations in pulse height being comparable to the average pulse heights there.

VI. SPATIAL RESOLUTION

For each wire the spatial resolution is calculated using residual distributions from a linear track fit. Separate distributions are accumulated over 4 mm drift distance intervals from 0 to 28 mm. A gaussian fit is applied to each distribution, and the resolution is obtained by averaging the fit results over all 8 (6) TDC (ICA) channels.

Position resolution measurements using TDC data were made for the narrow grid cell as a function of pressure, electron drift velocity, and threshold. Little dependence on threshold is observed until it is sufficiently large to cause a loss in efficiency. The electronic contributions to the resolution are negligible. Fig. 7 shows the squared resolution as a function of drift distance at 3 atmospheres pressure and 1 kilovolt/cm/atmos drift field for both cell designs. This is our standard operating point and has a drift velocity of 7.6 μm/nsec. The linear dependence of the squared resolution on drift distance is a well known consequence of electron diffusion. The linear fit shown in Fig. 7 has an intercept of 17.0 $\pm$1.1 μm and a slope of 29.8 $\pm$.7 $\mu m/\sqrt{cm}$ (Table 1). The intercept gives the resolution for a track passing near the grid plane and measures the contribution from track ionization statistics (small) and electron diffusion during the drift from the grid to the anode. The resolution in the wide grid chamber is about 15 percent better than the narrow grid because of the larger number of electrons competing

to be first.

TABLE 1

Summary of spatial resolution results.

	Intercept [μm]	Slope [$\mu m/\sqrt{cm}$]
Narrow Grid TDC	17.0 ± 1.1	$29.8 \pm .7$
Narrow Grid ICA	$17.9 \pm .9$	$23.3 \pm .5$
Wide Grid TDC	$12.9 \pm .7$	$25.8 \pm .3$
Wide Grid ICA	$15.6 \pm .5$	$23.2 \pm .2$

Fig. 8 illustrates the pressure dependence of the average resolution over the first 2 cm drift distance at an E/P of 1 kv/cm/atmos. A power law fit yields roughly a $P^{-.7}$ pressure dependence. Since the average chamber resolution is dominated by electron diffusion in the drift region, individual electron diffusion accounts for most of the pressure dependence, $P^{-.5}$, with the remainder due to the increased electron statistics.

The average resolution over the first 2 cm drift distance is nearly independent of drift velocity in the range of 5 to 10 μm/nsec (Fig. 9). Since the value of the electric field in the drift region only weakly effects the field seen by drifting electron inside the anode/grid gap, the anode region contributes roughly a constant resolution in time (about 2 nsec at 3 atmospheres). This produces a linear increase with drift velocity in the gap contribution to the resolution, which approximately cancels the resolution improvement caused by the decreasing electron diffusion over the average 2 cm drift distance.

We have studied spatial resolution in the ICA data with several centroid algorithms[5]: 1) pulse height weighted centroid of the first n bins above threshold; 2) weighted centroid of the first n bins where the weight is the product of the pulse height and a factor which falls off exponentially from the first bin above threshold; 3) an iterative pulse height weighted algorithm using an additional weight function which is constant for a fixed distance d_1 from the calculated

centroid on the previous iteration, and then linearly falls to zero at a distance d_0 from the calculated centroid.

At a fixed drift distance the two parameters of algorithms 2 and 3 can be optimized to give the same resolution, while the single parameter of the first algorithm can be adjusted to give nearly as good a result. The optimal parameters are found to vary with drift distance in a simple way consistent with diffusion broadening of the pulse with increasing drift distance. The squared resolution depends linearly on drift distance, and Table 1 lists the fit parameters for both the narrow and wide grid chambers. The result is nearly the same for the two chambers, although the optimal resolutions are obtained with somewhat different values of the weight parameters. More weight is given to later bins for the the narrow grid cell consistent with the smaller intrinsic contribution of the cell collection geometry to the pulse width. The ICA results are as good or better than the TDC results for all but the smallest drift distances.

VII. TRACK PAIR EFFICIENCY

We have used single track events to estimate the double track efficiency as a function of track separation by adding together the ICA data from two wires appropriately delayed to simulate closely spaced pulses. A hit finding algorithm optimized to find closely spaced hits efficiently and having a low probability to generate spurious hits is used. We first average the raw ICA samples over a 5 (2) bin interval for the wide (narrow) grid data. Then all extrema in this averaged data are found, and hits are defined as those maxima which are sufficiently larger than either adjacent minima.

Typical pulses in the narrow grid cell are roughly symetrical in shape and have little tail. Two tracks can be identified with 90% efficiency at 450 μm with a spurious hit rate on single track events of less than .7%. Pulses in the wide grid cell have a tail which extends about 1500 μm beyond the leading edge. Large fluctuations in the late arriving primary ionization clusters produce correspondingly large fluctuations in the pulse tail. Relatively tight cuts have

9

to be applied to reduce the spurious hit rate. Two tracks (see Fig. 10) can be identified with 90% efficiency at 900 μm separation with a spurious hit rate on single tracks of less than 2%.

VIII. CONCLUSION

In summary, we have built and tested full length prototypes of the drift chamber vertex detector for the Mark II Upgrade Detector using a jet-style drift cell augmented with focussing grids. Two cell designs have been studied. The narrow grid (wide grid) design can efficiently distinguish two tracks separated by 500 μm (1000 μm). Both designs operate reliably at 3 atmospheres pressure using a gas mixture of CO_2 and isobutane, and achieve spatial resolutions in the range of $20 - 50$ μm depending on the drift length.

IX. ACKNOWLEDGEMENTS

10

Figure Captions

1. Dimensions of the two drift cells: (a) wide grid; (b) narrow grid.

2. Electron drift trajectories in (a) the wide grid and (b) the narrow grid drift cells.

3. The line of constant drift time is shown for (a) the wide grid and (b) the narrow grid drift cells.

4. Measured deviations of wire positions from their nominal locations (a) ΔZ (out of the plane); (b) ΔX (in the plane).

5. Schematic view of wire terminations, showing the configuration of notches, epoxy, circuitry, and Macor, as explained in the text.

6. Average pulse shapes for narrow and wide grid drift cells, at short and long drift distances.

7. Squared resolution versus drift distance for the wide grid and narrow grid chambers, with fits to $\sigma^2 = \sigma_0^2 + (D\sqrt{x})^2$.

8. Average spatial resolution versus pressure.

9. Average spatial resolution versus drift velocity, at 2 and 3 bars.

10. Efficiency for detecting a second track as a function of the track separation for the wide grid chamber. The narrow grid chamber is 90% efficient at 450 μm separation.

References

1. Proposal for the Mark II at SLC, CALT-68-1015 (1983).

2. S. Bobkov *et al.*, Nucl. Instr. and Meth. 226 (1984) 375; V. Commichau *et al.*, Nucl. Instr. and Meth. A235 (1985) 267; D. Bettoni *et al.*, Nucl. Instr. and Meth. A236 (1985) 237.

3. W. Farr *et al.*, Nucl. Instr. and Meth. 156 (1978) 283; H. Drumm *et al.*, Nucl. Instr. and Meth. 176 (1980) 333.

4. U. Becker *et al.*, Nucl. Instr. and Meth. 214 (1983) 525.

5. W. Farr *et al.*, IEEE Trans. on Nucl. Sci. NS-30 (1983) 95; P. Bock *et al.*, Nucl. Instr. and Meth. A242 (1986) 237; D. Schaile *et al.*, Nucl. Instr. and Meth. A242 (1986) 247.
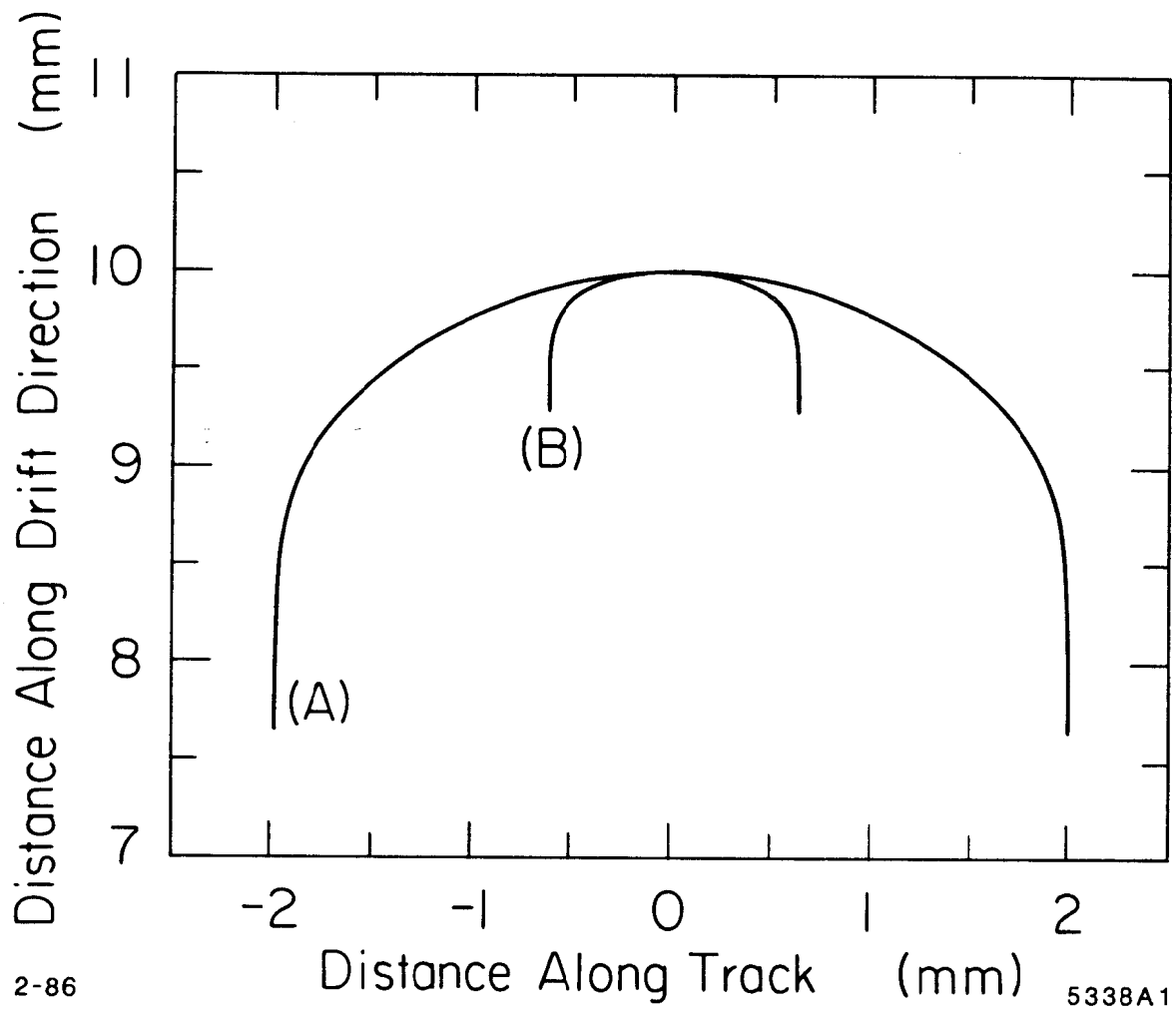
× 20 μm Sense Wire

● 152 μm Grid & Potential Wires

(a) |←— 2.4 mm —→|

●   ●   ●

2.0 mm

                          ×

●   ●   ●

(b) |←1.7 mm→|

800 μm   ●   ●   ●

550 μm   ●   ●

          ●   ●

                 ×

2.0 mm   ●   ● ←— Inner Grid

          ●   ● ←— Middle Grid

          ●   ●   ● ←— Outer Grid

2-86   5338A7

Fig. 1

(a)

(b)

Fig. 2

Fig. 3

2-86   5338A1

2-86

WIRE NUMBER

5338A8

Fig. 4

Notches

Anode Plane

G10 Circuit Board

Epoxy

Macor

Potential Wire Bus

Sense Wires

Lower Grid Plane

Amp Connections

Epoxy

Kapton Circuitry

Macor

5338A9

2-86

Fig. 5

Fig. 6

Fig. 7

Fig. 8

Fig. 9

Fig. 10

2-86

5338A10